Monthly Notices
of the
ROYAL ASTRONOMICAL SOCIETY

MNRAS **490,** 2124–2138 (2019)
Advance Access publication 2019 September 13

doi:10.1093/mnras/stz2565

SDSS-IV MaNGA: the inner density slopes of nearby galaxies

Ran Li [1,2,3]★ Hongyu Li,[1,2,3] Shi Shao [4] Shengdong Lu,[1,2] Kai Zhu,[1,2] Chunxiang Wang,[1,2] Liang Gao,[1,2,3,4] Shude Mao,[5,1] Aaron A. Dutton [6] Junqiang Ge,[1] Yunchong Wang [5] Alexie Leauthaud [7] Zheng Zheng,[1] Kevin Bundy[7] and Joel R. Brownstein [8]

[1]*National Astronomical Observatories, Chinese Academy of Sciences, 20A Datun Road, Chaoyang District, Beijing 100012, China*
[2]*Key laboratory for Computational Astrophysics, National Astronomical Observatories, Chinese Academy of Sciences, Beijing 100012, China*
[3]*School of Astronomy and Space Science, University of Chinese Academy of Science, Beijing 100049, China*
[4]*Institute for Computational Cosmology, Department of Physics, University of Durham, South Road, Durham DH1 3LE, UK*
[5]*Physics Department and Tsinghua Centre for Astrophysics, Tsinghua University, Beijing 100084, China*
[6]*New York University Abu Dhabi, PO Box 129188, Abu Dhabi, United Arab Emirates*
[7]*Department of Astronomy and Astrophysics, University of California, Santa Cruz, 1156 High Street, Santa Cruz, CA 95064, USA*
[8]*Department of Physics and Astronomy, University of Utah, 115 S. 1400 E., Salt Lake City, UT 84112, USA*

Accepted 2019 September 9. Received 2019 September 9; in original form 2019 March 18

ABSTRACT

We derive the mass-weighted total density slopes within the effective (half-light) radius, γ', for more than 2000 nearby galaxies from the SDSS-IV (Sloan Digital Sky Survey IV) MaNGA survey using Jeans-anisotropic-models applied to integral field unit observations. Our galaxies span a wide range of the stellar mass ($10^9\ \mathrm{M}_\odot < M_* < 10^{12}\ \mathrm{M}_\odot$) and the velocity dispersion ($30\ \mathrm{km\,s^{-1}} < \sigma_v < 300\ \mathrm{km\,s^{-1}}$). We find that for galaxies with velocity dispersion $\sigma_v > 100\ \mathrm{km\,s^{-1}}$, the density slope has a mean value $\langle\gamma'\rangle = 2.24$ and a dispersion $\sigma_\gamma = 0.22$, almost independent of velocity dispersion, consistent with previous lensing and stellar dynamical analysis. We also quantitatively confirm with high accuracy a turnover in the γ'–σ_v relation is present at $\sigma \sim 100\ \mathrm{km\,s^{-1}}$, below which the density slope decreases rapidly with σ_v, consistent with the results reported by previous analysis of ATLAS^{3D} survey. Our analysis shows that a large fraction of dwarf galaxies (below $M_* = 10^{10}\ \mathrm{M}_\odot$) have total density slopes shallower than 1, which implies that they may reside in cold dark matter haloes with shallow density slopes. We compare our results with that of galaxies in hydrodynamical simulations of EAGLE, Illustris, and IllustrisTNG projects, and find all simulations predict shallower density slopes for massive galaxies with high σ_v. Finally, we explore the dependence of γ' on the positions of galaxies in haloes, namely centrals versus satellites, and find that for the same velocity dispersion, the amplitude of γ' is higher for satellite galaxies by about 0.1.

Key words: galaxies: evolution – galaxies: formation – galaxies: kinematics and dynamics – galaxies: structure.

1 INTRODUCTION

Various *N*-body simulations have shown that the density structure of dark matter haloes in a universe formed with pure cold dark matter follows a universal NFW form (Navarro, Frenk & White 1996b, 1997). The density profile, $\rho(r)$, of a dark matter halo scales with r^{-1} for the inner part and scales with r^{-3} for the outer part, independent of the mass of the halo.

In the real Universe, the inner density profile depends on both the dark matter and baryons. Baryons cool and condense at the centre of dark matter haloes and form galaxies. The baryons often contribute a significant amount of mass within the half-light radius (e.g. Courteau & Dutton 2015). The condensation of the baryonic matter can also modify the central potential of the dark matter halo. If the condensation process is slow comparing to the local dynamical time-scale of the dark matter halo, then the response of the dark matter halo can be described by an adiabatic contraction effect (e.g. Blumenthal et al. 1986; Gnedin et al. 2004; Gustafsson, Fairbairn & Sommer-Larsen 2006). In a realistic galaxy, the contraction may not be adiabatic, thus the description of the contraction is more complex. On the other hand, stellar and active galactic nucleus feedback can create rapid gas outflows that may induce an expansion effect at the halo centre, resulting in a central core in the dark

★ E-mail: ranl@bao.ac.cn

matter density profiles (Dehnen 2005; Read & Gilmore 2005; Duffy et al. 2010; Pontzen & Governato 2012). Accurate measurement of density profiles of galaxies thus provides a critical constraint on galaxy formation models.

In observations, the inner density profile of galaxies are best measured through stellar kinematics and gravitational lensing effects (e.g. Koopmans et al. 2009; Auger et al. 2010; Cappellari et al. 2013; Sonnenfeld et al. 2013; Newman et al. 2015; Poci et al. 2017; Huang et al. 2018; He et al. 2019). The Sloan Lens Advanced Camera for Surveys (SLACS) project studied a sample of 73 galaxy–galaxy lensing systems with lens stellar masses $M_* > 10^{11}$ $M_\odot$ (Koopmans et al. 2009; Auger et al. 2010) and found that the mean of power-law density slope of the total mass within the Einstein radius is $\gamma_{\rm tot} = 2.078$, very close to a singular-isothermal-sphere profile.[1] The dark matter and baryon profiles have very different density slopes, and both slopes vary from galaxy to galaxy (e.g. Auger et al. 2010; Bruderer et al. 2016). The close to the isothermal value implies that both baryons and dark matter contribute non-negligible fractions to the mass within the effective radii of massive elliptical galaxies. A quantitative explanation of the mean and scatter of the slope requires appropriate coupling mechanisms between two components. This is sometimes referred to as the 'bulge-halo conspiracy' (Dutton & Treu 2014).

Compared with rare strong lensing systems, dynamical modelling methods can be applied to much larger samples of galaxies. With recent developments in integral field unit (IFU) surveys, e.g. ATLAS^{3D} (Cappellari et al. 2011), CALIFA (Sánchez et al. 2012), MASSIVE (Ma et al. 2014), SAMI (Bryant et al. 2015) and SDSS-IV MaNGA (Bundy et al. 2015), accurate mass density profiles for large statistical samples of galaxies are becoming available. Cappellari et al. (2013) constructed anisotropic dynamical models for 260 early-type galaxies in the ATLAS^{3D} sample. Follow-up analysis (Poci, Cappellari & McDermid 2017) shows that the inner total density slopes of these early-type galaxies have a mean value of $\gamma'_{\rm tot} = 2.193$, with a scatter of $\sigma_{\gamma'} = 0.174$, which is slightly steeper than the SLACS strong lensing results. The total density slope is almost a constant for galaxies with effective velocity dispersion $\log\sigma_v > 2.1$ km s^{-1}, and becomes shallower gradually with σ_v for galaxies with $\log\sigma_v < 2.1$ km s^{-1} (also see the review of Cappellari 2016). Using the sample of early-type galaxies from ATLAS^{3D} and SPIDER (La Barbera et al. 2010), Tortora et al. (2014) found $\gamma'_{\rm tot} \sim 2$, increasing gradually with velocity dispersion. For massive clusters, recent observations combining stellar dynamics and gravitational lensing effects show that the total inner density slope drops gradually to 1.7 (Auger et al. 2010; Newman, Ellis & Treu 2015).

In this paper, we make use of IFU observations from the MaNGA survey to study the density slopes for nearby galaxies with a wider range of galaxy masses and morphologies than previous studies. We derive the galaxy density profiles using mass models of galaxies in MaNGA DR14 (Abolfathi et al. 2018), which are derived by Li et al. (2018) with Jeans anisotropic model (JAM; Cappellari 2008), and investigate the relation between density slopes and the galaxy stellar mass, the stellar surface density, the velocity dispersion and other properties.

The structure of the paper is as follows. In Section 2, we outline the MaNGA data we use. In Section 3, we briefly introduce our dynamical modelling technique, and in Section 4, we present our main results, and finally in Section 5, we summarize our results and present a short discussion.

2 MANGA GALAXIES

The galaxy sample of this project comprises 2778 galaxies from MaNGA survey in SDSS-IV DR14 (Abolfathi et al. 2018), covering a stellar mass range of $10^9 < M_* < 10^{12}$ $M_\odot$, including both early-type and late-type galaxies. Throughout this work, we define early-type galaxies as those with Sérsic index $n_{\rm sc} > 2.5$, and the remainders as late-type galaxies. Sérsic indices are taken from the NASA-Sloan Atlas, NSA catalogue.[2] From the DR14 sample, we exclude merging galaxies (or close galaxy pairs), galaxies with a significant disturbance, and galaxies with strong bars or strong spiral arms. We also exclude galaxies of low data quality, defined as having less than 100 Voronoi with S/N > 10 bins. In total, we have 2110 galaxies in our final sample, with 952 early-type galaxies and 1158 late-type galaxies.

We use the IFU spectra extracted with the official data reduction pipeline (DRP Law et al. 2016) and the kinematic data extracted with the official data analysis pipeline (Westfall et al. 2019). The kinematic information are obtained by fitting absorption lines using the PPXF software (Cappellari & Emsellem 2004; Cappellari 2017).

In this paper, we derive the stellar mass of each galaxy by multiplying their total luminosity in SDSS r-band by their mean stellar mass-to-light ratio within the effective radius, $M_*^{\rm SPS}/L^r$, derived by Li et al. (2018, see online table), in which the mass-to-light ratio is obtained by fitting spectra with stellar population templates using PPXF software (Cappellari & Emsellem 2004) with the MILES-based (Sánchez-Blázquez et al. 2006) SPS models of Vazdekis et al. (2010) and the Salpeter (1955) initial mass function. Before spectrum fitting, the data cubes are Voronoi binned to S/N = 10 (Cappellari & Copin 2003). In Appendix B, we show that for a given galaxy, the exact choice of the Voronoi bin number wont' affects the results of the JAM model.

We refer readers to Li et al. (2018) for details of stellar mass calculation. For MaNGA-related information, readers are referred to the following papers: SDSS-IV technical summary (Blanton et al. 2017), MaNGA instrumentation (Drory et al. 2015), observing strategy (Law et al. 2015), sample design (Wake et al. 2017), spectrophotometric calibration (Smee et al. 2013; Yan et al. 2016a), survey execution and initial data quality (Yan et al. 2016b), and a SDSS telescope introduction can be found in Gunn et al. (2006).

3 DYNAMICAL MODEL

Our mass models of MaNGA galaxies are built by the method described in Li et al. (2018) with the multi-Gaussian Expansion (MGE Emsellem, Monnet & Bacon 1994; Cappellari 2002) technique, in conjunction with the JAM (Cappellari 2008). Below, we briefly summarize the method.

We assume that the stellar system of an observed galaxy can be approximated by a steady axisymmetric system of collisionless particles, and can be described by Jean Equations Jeans (1922) and Binney & Tremaine (1987). In a cylindrical coordinate, we can write

[1] Note that throughout this paper we adopt the convention that density slopes are positive, i.e. $\rho \propto r^{-\gamma}$.

[2] Downloaded from https://academic.oup.com/mnras/article-abstract/476/2/1765/4848297 by National Astronomical Observatory user on 2018 June 26.

the Jeans equations as

$$\frac{\nu\overline{v_R^2} - \nu\overline{v_\phi^2}}{R} + \frac{\partial\left(\nu\overline{v_R^2}\right)}{\partial R} + \frac{\partial(\nu\overline{v_R v_z})}{\partial z} = -\nu\frac{\partial\Phi_{\rm tot}}{\partial R}, \quad (1)$$

$$\frac{\nu\overline{v_R v_z}}{R} + \frac{\partial\left(\nu\overline{v_z^2}\right)}{\partial z} + \frac{\partial(\nu\overline{v_R v_z})}{\partial R} = -\nu\frac{\partial\Phi_{\rm tot}}{\partial z}, \quad (2)$$

where

$$\nu\overline{v_k v_j} \equiv \int v_k v_j f \, {\rm d}^3\boldsymbol{v}, \quad (3)$$

where f is the distribution function of the stars, $\Phi_{\rm tot}$ is the gravitational potential, and ν is the luminosity density (see equation 8).

Following Cappellari (2008), we assume (i) the velocity dispersion ellipsoid aligns with the cylindrical coordinate system ($\overline{v_R v_z} = 0$) and (ii) the anisotropy parameter β_z is a constant in the meridional plane, where

$$\beta_z = 1 - \frac{\overline{v_z^2}}{\overline{v_R^2}}. \quad (4)$$

Thus, the Jeans equations reduce to

$$\frac{b\,\nu\overline{v_z^2} - \nu\overline{v_\phi^2}}{R} + \frac{\partial\left(b\,\nu\overline{v_z^2}\right)}{\partial R} = -\nu\frac{\partial\Phi_{\rm tot}}{\partial R}, \quad (5)$$

$$\frac{\partial\left(\nu\overline{v_z^2}\right)}{\partial z} = -\nu\frac{\partial\Phi_{\rm tot}}{\partial z}. \quad (6)$$

We integrated the intrinsic velocity moments along the line of sight to obtain the projected second velocity moment with a free parameter θ_i to describe the inclination angle. Then we can constrain our mass model by comparing the observed flux-weighted line-of-sight root-mean-square velocity $v_{\rm rms} = \sqrt{v^2 + \sigma^2}$ with the theoretical prediction.

Our mass model consists of a stellar component and a spherical dark matter halo. We assume that the stellar component follows the distribution of r-band surface brightness, $\Sigma(x', y')$, of the galaxy, which can be expressed as a summation of a series of elliptical Gaussian functions:

$$\Sigma(x', y') = \sum_{k=1}^{N} \frac{L_k}{2\pi\sigma_k^2 q_k'} \exp\left[-\frac{1}{2\sigma_k^2}\left(x'^2 + \frac{y'^2}{q_k'^2}\right)\right], \quad (7)$$

where L_k is the total luminosity of the kth Gaussian component with dispersion σ_k along the major axis, N is the total number of Gaussians used in the expansion, and q_k' is the axial ratio of the kth elliptical Gaussian distribution. We use the MGE_FIT_SECTORS[3] software (Cappellari 2002) to perform MGE fitting. For each galaxy, we derive its effective radius $R_{\rm e}$ using the best-fitting MGE model of the galaxy.

Following Cappellari et al. (2013), we assume an oblate axisymmetric shape for the 3D luminosity density of the galaxies. Under this assumption, we can obtain an unique deprojected 3D luminosity density for a given inclination angle, as

$$\nu(R, z) = \sum_{k=1}^{N} \frac{L_k}{(\sqrt{2\pi}\sigma_k)^3 q_k} \exp\left[-\frac{1}{2\sigma_k^2}\left(R^2 + \frac{z^2}{q_k^2}\right)\right], \quad (8)$$

[3]Available from http://www-astro.physics.ox.ac.uk/~mxc/software.

where L_k and σ_k are the same parameters in equation (7), and q_k is the 3D axial ratio of each Gaussian component, related to the projected value q_k' as

$$q_k = \frac{\sqrt{q_k'^2 - \cos^2 i}}{\sin i}, \quad (9)$$

The stellar mass distribution in 3D can then be obtained by multiplying a constant mass-to-light ratio, M_*/L.

The mass distribution of dark matter haloes is assumed to follow a spherical gNFW profile, where density $\rho_{\rm DM}$ can be written as

$$\rho_{\rm DM} = \rho_{\rm s}\left(\frac{r}{R_{\rm s}}\right)^{-\gamma}\left(\frac{1}{2} + \frac{r}{2R_{\rm s}}\right)^{\gamma-3}, \quad (10)$$

where $\rho_{\rm s}$ is the characteristic density and $R_{\rm s}$ is the scale radius. These two parameters are treated as free parameters during fitting.

We use EMCEE, a PYTHON MCMC package (Foreman-Mackey et al. 2013) to sample the posterior distribution of our model parameters. Previous simulations have shown that our method can provide a robust description for total mass profile of galaxies (Li et al. 2016).

In our fiducial model, we assume light traces mass strictly, i.e. the mass-to-light ratio for the stellar component is a constant, independent of the radius. In the real Universe, this assumption is not strictly true (e.g. Poci et al. 2017; Li et al. 2018; Sonnenfeld et al. 2018; Wasserman et al. 2018). Specifically, a recent research by Sonnenfeld et al. (2018), using gravitational lensing data, derived a mass-to-light ratio of -0.24 for early-type galaxies in the SLACS sample, the exact value of which depends on choice of the dark matter halo model. More directly, Li et al. (2018) derived the average mass-to-light ratio gradient $\Delta\log(\Gamma)/\Delta\log(R/R_{\rm e})$ between $R_{\rm e}/8$ and $R_{\rm e}$ using SPS with a Salpeter IMF for MaNGA galaxies in SDSS DR14, and found that the mass-to-light ratio gradient varies from ~ -0.2 for massive galaxies to ~ 0.1 for low-mass galaxies.

In our model, if the mass-to-light ratio of a MaNGA galaxy is not constant, the best-fitting dark matter density profile will be biased, but the recovery of the total density profile will not be affected given the flexibility of our total mass model. Two validation tests are shown in the Appendix. In Appendix A, we perform the JAM analysis with an alternative mass model, where the total density profile follows a double power-law model with no prior knowledge for stellar mass distribution. The resulting slopes of the total density profile agree well with that derived from our fiducial model. In Appendix B, we show that total density slopes can be recovered accurately for the mock observations made from hydrodynamical cosmological simulation. In this paper, we always show the results using total mass density profile, thus our conclusions are not affected by the mass-to-light ratio gradient.

4 OBSERVATIONAL RESULTS

4.1 Inner density slopes

Following Dutton & Treu (2014), we define the mass-weighted density slope within the effective radius $R_{\rm e}$ as

$$\gamma' \equiv -\frac{1}{M(R_{\rm e})}\int_0^{R_{\rm e}} 4\pi r^2\rho(r)\frac{{\rm d}\log\rho}{{\rm d}\log r}{\rm d}r = 3 - \frac{4\pi R_{\rm e}^3\rho(R_{\rm e})}{M(R_{\rm e})}, \quad (11)$$

where $\rho(r)$ is total mass density of the galaxy and $M(R)$ is the total mass enclosed in a sphere with radius R, which we calculate using

MGE_RADIAL_MASS and MGE_RADIAL_DENSITY subroutines in the JAM package.[4]

In Fig. 1, we show the results of JAM analysis for 25 MaNGA galaxies with different masses. In each subplot, the upper panels show the observed (left) and recovered (right) distribution $v_{\rm rms}$, and the lower panels show the best-fitting density profile of stars (yellow), dark matter (red), and total density profile (blue).

In the top panel of Fig. 2, we present γ' as a function of σ_v, the luminosity-weighted velocity dispersion within $R_{\rm e}$ for all the galaxies in our MaNGA sample. The colour of data points show the Sérsic index of the light profiles. For galaxies with $\sigma_v < 100\,{\rm km\,s^{-1}}$, the density slope increases rapidly from 0.5 to 2, while for galaxies with $\sigma_v \geq 100\,{\rm km\,s^{-1}}$ the inner density slopes stay roughly constant at a value of 2.24, slightly steeper than the isothermal slope (2). We find that the γ'–σ_v relation can be described with the following formula

$$\gamma' = A_0 \frac{(\sigma_v/\sigma_0)^{\alpha}}{(1+\sigma_v/\sigma_0)^{\beta-\alpha}}\,, \tag{12}$$

with $\{A_0, \sigma_0, \alpha, \beta\} = \{19.83, 116.62, 2.1, 5.44\}$.

In the middle and bottom panels of Fig. 2, we divide our galaxies into early-type and late-type according to their Sérsic index and show their γ'–σ_v relations, respectively. For early-type galaxies ($n_{\rm sc} \geq 2.5$), the inner density slope is almost a constant for galaxies with $\sigma_v > 100\,{\rm km\,s^{-1}}$. The mean value of the inner total density slope is $\langle\gamma'\rangle = 2.24$, with a dispersion $\sigma_\gamma = 0.22$, agreeing well with previous observations from lensing and stellar dynamics. For those early-type galaxies with low-velocity dispersion, the total density slope increases rapidly with σ_v. For late-type galaxies, the total γ' also increases with σ_v, the behaviour of which is similar to early-type galaxies of the same σ_v range.

Note that, we do not put any cut on the velocity dispersion for our sample selection. Westfall et al. (2019) estimates that the standard deviation of uncertainties on stellar velocity dispersion is 20–30 per cent for a Voronoi bin with S/N >10 and intrinsic stellar velocity dispersion of 35 $\rm km\,s^{-1}$. In each panel of Fig. 2, we plot a vertical line at 35 $\rm km\,s^{-1}$. Almost all our galaxies have $\sigma_v > 35\,{\rm km\,s^{-1}}$.

In Fig. 3, we show the relation between γ' and the stellar mass $M_*^{\rm SPS}$. In the upper panel, we plot γ' versus $M_*^{\rm SPS}$ for each MaNGA galaxy using scatter points. The colours of points represent the effective radius of each galaxy in kpc. The black solid circles represent the mean of the relation and the two dashed lines enclose 70 per cent of the galaxies at each mass. For reference, we show the flux-weighted r-band brightness slope of the stars, γ'_L, as a function of stellar mass using red empty circles. The average slope of the luminous matter is always steeper than the average total mass slope, implying that the average total slope is an upper limit to the average density slope of the dark matter within the effective radius. In the lower panel of the figure, we plot $f_{\rm dm}$, the dark matter to total mass fraction with $R_{\rm e}$, which is derived from JAM model. The density slope grows almost linearly with $M_*^{\rm SPS}$ in the range of $[10^{10}, 10^{11}]$ $\rm M_\odot$, while for the most massive galaxies, γ' goes flat with stellar mass with a mean of ∼2.15.

One can find that the galaxies of larger sizes tend to have lower γ' for the same stellar mass. Larger effective radii affect the total density slope in two ways: a more extended distribution of stellar mass that results in a shallower stellar density slope; more dark matter included into the calculation of γ', because the dark matter usually takes larger fraction of total mass at the outer part of a galaxy. Since the dark matter density slopes are much shallower than those of stellar mass, the latter effect also drives the total density slope to a lower value.

For galaxies more massive than 10^{11} $\rm M_\odot$, the amplitude of mean γ'–$M_*^{\rm SPS}$ flattens. From the lower panel of Fig. 3, we find these galaxies contain on average ∼ 10 per cent dark matter within $R_{\rm e}$, thus their total density slopes are almost identical as their stellar density slopes, which is roughly constant at this mass range (red empty circles in the upper panel of Fig. 3).

In a recent paper, Tortora et al. (2019) analysed the kinematic data of spiral galaxies from SPARC data base (Lelli, McGaugh & Schombert 2016), massive ellipticals from SPIDER sample, and dwarf ellipticals from SMACKED sample (Tortora, La Barbera & Napolitano 2016), and presented a U-shape behaviour for the dark matter fraction and total mass density slopes with stellar mass, with the steepest total mass density slope (and lowest dark matter fraction) in galaxies of 3×10^{10} $\rm M_\odot$. At the high-mass end, the total density slopes or their galaxies are shallower for more massive galaxies in their sample, while the trend is not observed in our sample.

Interestingly, we find that the mean total density slopes for galaxies less massive than 10^{10} $\rm M_\odot$ are below 1.0, while their luminosity profile slopes still possess a mean value of ∼1.7 and the JAM modelling shows these galaxies are dominated by dark matter within the effective radius. A direct implication of these results is that many galaxies in this mass range reside in dark matter haloes with shallow inner density slopes even shallower than 1. In the context of CDM, dissipationless simulations predict steeper slopes than 1, thus the shallow slopes we find for MaNGA dwarf galaxies implies their dark matter haloes have expanded.

The M_*/L gradient can also contribute to the shallow total density profile. However, Li et al. (2018) has shown that the M_*/L gradient of MaNGA galaxies with $M_*^{\rm SPS} < 10$ is ∼0.1 (positive sign means the central value is higher). Thus, the observed shallow total density profile is not likely to be explained purely by the gradient of M_*/L.

One caveat of the results is that the galaxies are all dwarf galaxies of relatively small physical size and luminosity, thus may suffer larger systematics in JAM modelling. However, we find the density slopes of the dwarf galaxies not correlating with their apparent sizes. Dwarf galaxies with relatively larger apparent size can still have shallow density slopes. In Fig. 4, we show six examples of galaxies with total density slopes $\gamma' < 1$. In the upper panel of each subplot, we show the distribution of observed root-mean-squared velocity $v_{\rm rms}$, and the $v_{\rm rms}$ reconstructed with the JAM. In the lower panels, we show the density profiles derived from the JAM model. For each galaxy, we plot the best-fitting density profile with solid line, and its 1σ error with dashed line. The yellow, red, and blue lines show profiles of stellar, dark matter, and total mass, respectively. For these examples, we can find they all have steep gradients of $v_{\rm rms}$, with high $v_{\rm rms}$ at $R_{\rm e}$ and low $v_{\rm rms}$ at inner part, which requires flat total mass density slopes within $R_{\rm e}$.

In Fig. 5, we show the relation between γ' and $\Sigma_*^{\rm SPS}$, the stellar surface density averaged within $R_{\rm e}$. Blue points show the data of each galaxy. The red shading shows the region enclosing 70 per cent data points and the black line shows the mean of the relation. We find the relation between γ' and $\Sigma_*^{\rm SPS}$ changes slope at $\sim 10^9\,{\rm M_\odot/kpc^2}$, and we can fit the relation with

$$\gamma' = \begin{cases} a_1 \log M + b_1 & \text{if } M < M_s \\ a_2 \log M + b_2 & \text{if } M >= M_s \end{cases}\,, \tag{13}$$

[4]Available from http://www.astro.physics.ox.ac.uk/mxc/software.

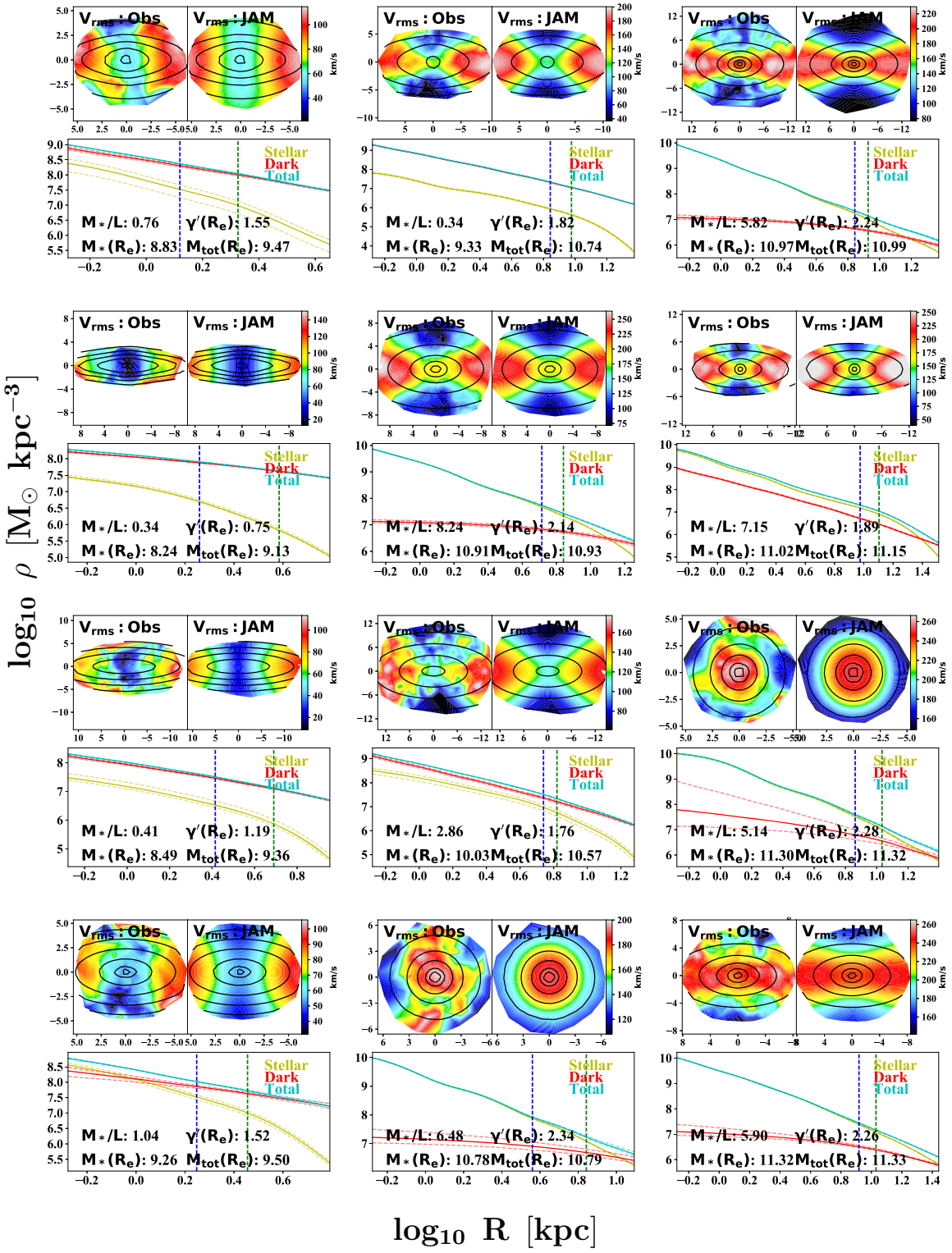

Figure 1. The figure shows the JAM fitting results for 24 examples of MaNGA galaxies. In each subplot, the upper panels show the observed (left) and best-fitting (right) distribution of $v_{\rm rms}$, and the lower panels show the best-fitting density profile of stars (yellow), dark matter (red) and total density profile (blue). The solid lines show the best-fitting profile, while the dashed lines show the 1σ errors. In each subplot, we marked the best-fitting value of M_*/L, $M_{\rm tot}$, M_*, and γ from JAM. The stellar mass of the galaxies increases from left to right.

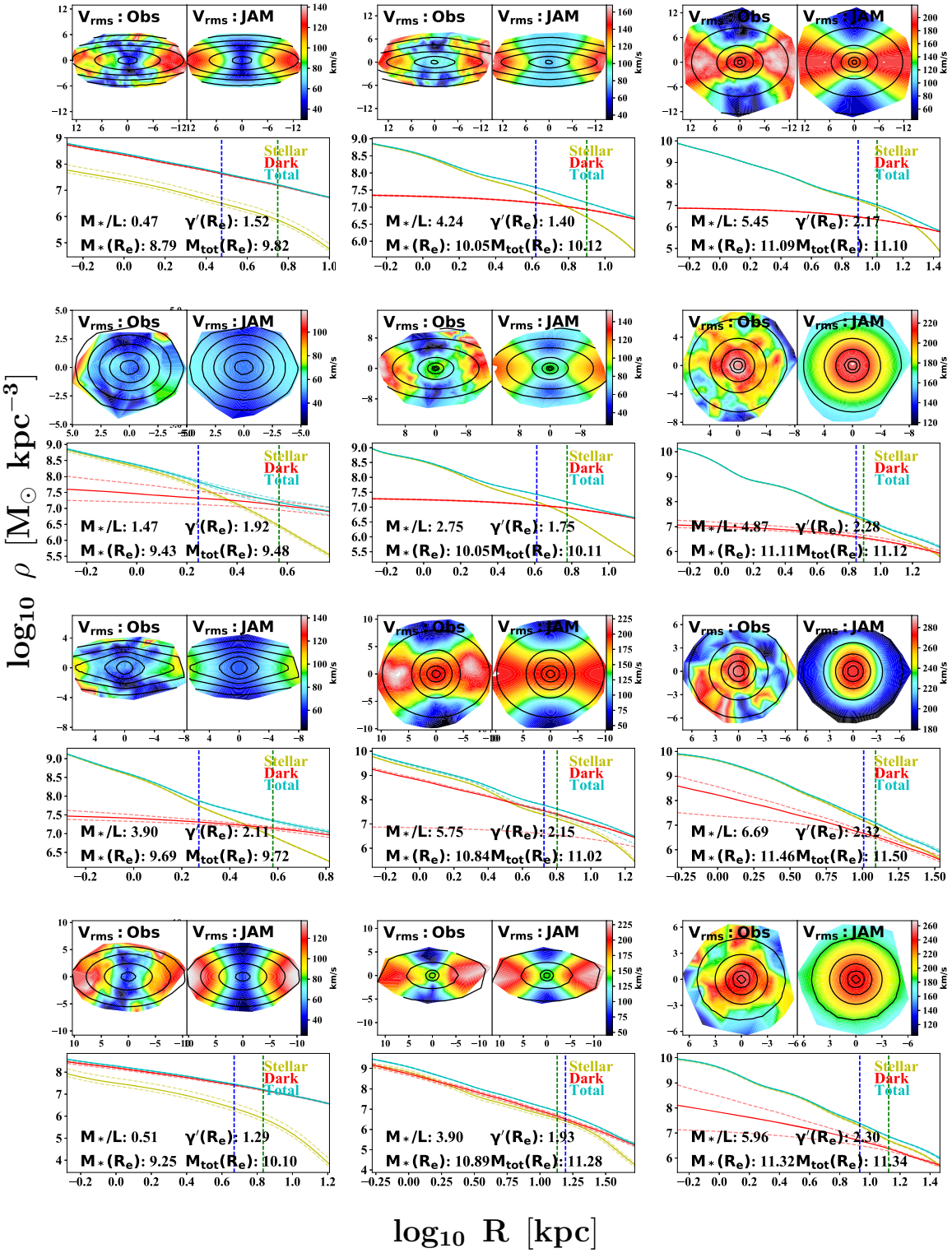

Figure 1 – *continued*

where $\{M_s, a_1, b_1, a_2, b_2\} = \{8.90, 0.56, -3.11, 1.56, -12.27\}$.

In Fig. 6, we compare our density slopes with predictions from hydrodynamical simulations: EAGLE (Crain et al. 2015; Schaye et al. 2015) and Illustris (Genel et al. 2014; Vogelsberger et al. 2014a,b) and IllustrisTNG project (Marinacci et al. 2018; Naiman et al. 2018; Nelson et al. 2018, 2019; Pillepich et al. 2018; Springel et al. 2018). For IllustrisTNG simulations, we only use the simulation run in cubic volume of 100 Mpc side length (TNG100, hereafter). In these simulations, we select all galaxies with stellar mass $M_* > 10^9\,\mathrm{M}_\odot$, and calculate their total γ' within the 3D

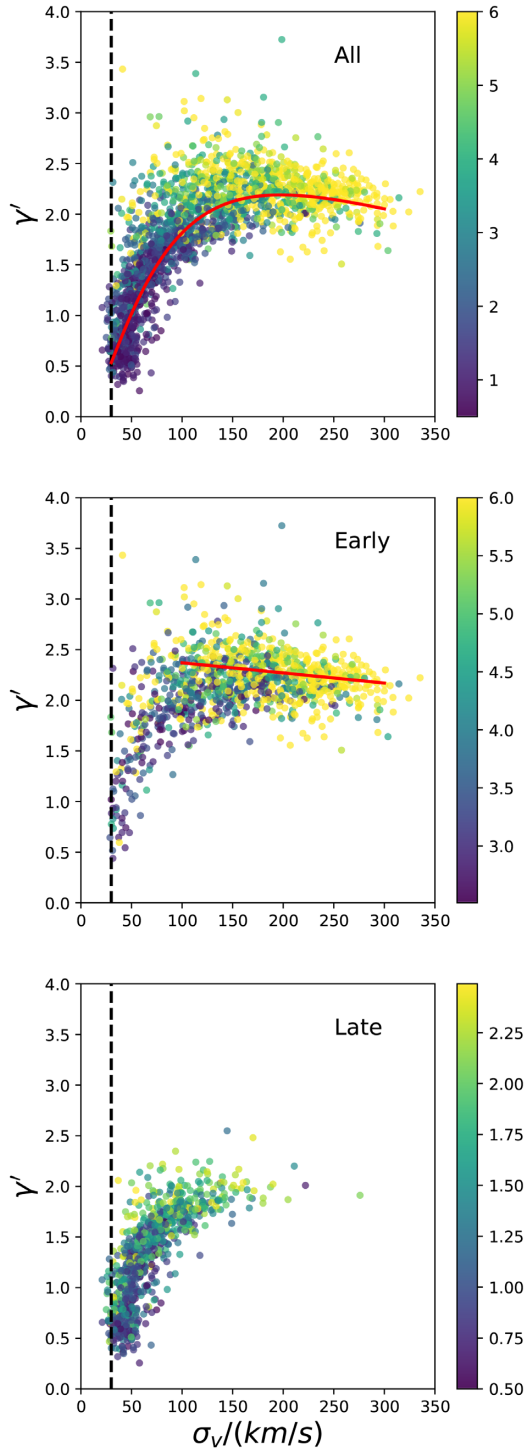

Figure 2. The figure shows $\gamma^{'}$ as a function of σ_v. The colour of the data points show the Sérsic index of the light profile, $n_{\rm sc}$. The top panel shows the results for all samples, the middle panel shows the results for early-type galaxies ($n_{\rm sc} >$ =2.5), and the bottom panel shows the results of late-type galaxies ($n_{\rm sc} < 2.5$). The red solid line in the top panel shows a best-fitting model of equation (12). In the middle panel, the red solid line shows a linear fit for data points with $\sigma_v > 100\,{\rm km\,s^{-1}}$, $\gamma' = 2.47 - 0.1\frac{\sigma_v}{100\,{\rm km\,s^{-1}}}$. In each panel, we plot a vertical line at 35 $\rm km\,s^{-1}$.

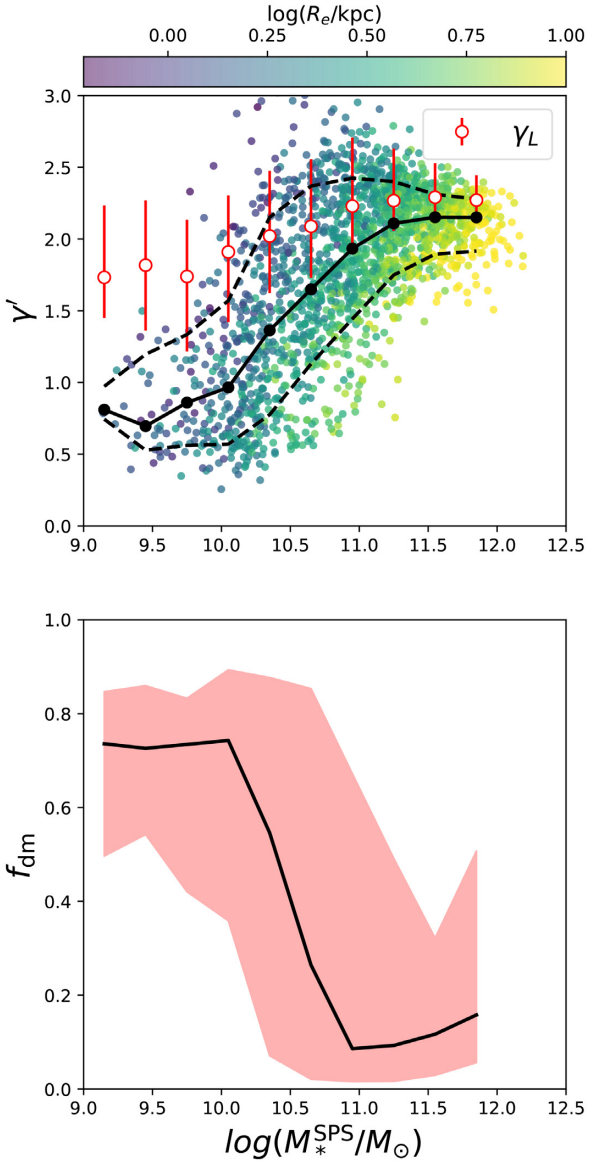

Figure 3. In the upper panel, we show $\gamma^{'}$ as a function of galaxies' stellar mass, $M_*^{\rm SPS}$. The colours of scatter points show the effective radius of these galaxies. The black solid circles represent the mean of the relation and the dashed lines show the region that encloses 70 per cent sample. For reference, we show the flux-weighted r-band brightness slope, γ_L' as a function of $M_*^{\rm SPS}$ using red empty circles, with error bars showing the region enclosing 70 per cent of sample. In the lower panel, we show the $f_{\rm dm}$–$M_*^{\rm SPS}$ relation with black solid line. The red shadow shows the region that encloses 70 per cent of the sample.

radius that equals to their projected half-light radius. To calculate the projected half-light radius, we assume a constant mass-to-light ratio.

In general, all simulations reproduce the total density slope of galaxies reasonably well. However, all of the simulations predicts a mean $\gamma^{'}$ slightly smaller than 2 for the galaxies with high σ_v, which is shallower than the observed value of 2.24. At the low σ_v end, the Illustris simulation can reproduce the shallow density slopes in observations, while the total density slopes predicted by EAGLE simulation are significantly higher than the observed values. For the TNG100 simulation, the density slopes spread a wide range for

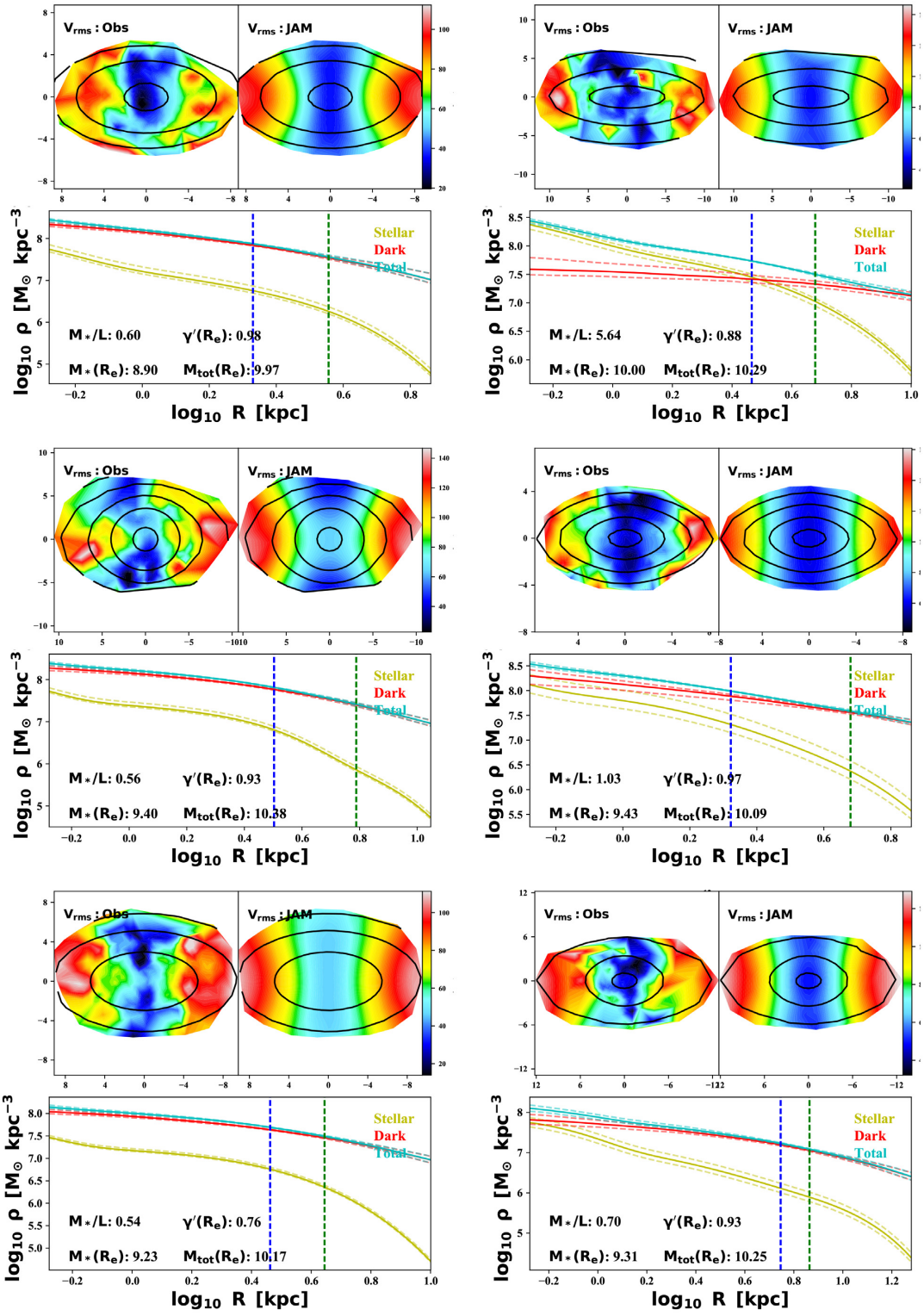

Figure 4. In this figure, we show six examples of galaxies with total density slopes $\gamma^{'} < 1$. In the upper panel of each subplot, we show the observed velocity field, and the velocity field reconstructed with the JAM. The unit for the axes is arcsec. In the lower panel, we show the density profiles derived from the JAM model. For each galaxy, we plot the best-fitting density profile with solid line, and its 1σ error with dashed line. The yellow, red, and blue lines show profiles of stellar, dark matter, and total mass, respectively. The vertical lines show the position of R_e and $2R_e$. In each subplot, we also mark the quantities derived using JAM, including stellar mass-to-light ratio, the total density slope, the total mass enclosed within R_e, and the total stellar mass enclosed within R_e.

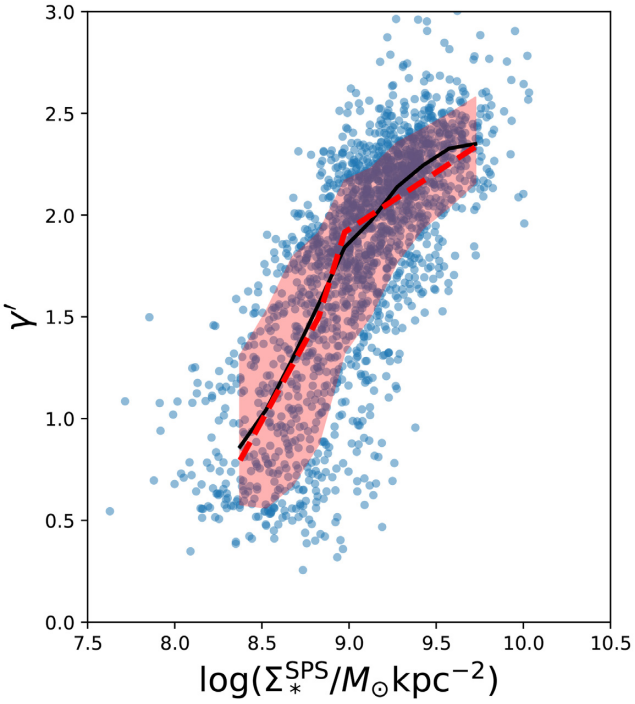

Figure 5. The figure shows the relation between γ' and stellar surface density $\Sigma_*^{\rm SPS}$. Blue points show the data of each galaxy. The red shadow shows the region enclosing 70 per cent data points and the black line shows the mean of the relations. The red dashed line in the right-hand panel shows the best-fitting double linear function for $\gamma' - \Sigma_*^{\rm SPS}$.

low σ_v galaxies. The turnover of γ'–σ_v relation at $\sigma \sim 100$ km s^{-1} is recovered in the Illustris, while the EAGLE and the TNG100 simulation predict flat γ'–σ_v relations.

In this figure, we also plot the total density slopes from strong lensing of the SLACS (Auger et al. 2010) and the JAM modelling results for ATLAS^{3D} early-type galaxies (Poci et al. 2017). Our results are consistent with previous strong lensing observations and ATLAS^{3D} results for early-type galaxies with $\sigma_v > 100$ km s^{-1}. We also confirm quantitatively the existence of the break in the relation at σ_v 100 km s^{-1} that was reported previous with ATLAS^{3D} sample (Cappellari 2016; Poci et al. 2017), but our analysis derives a lower amplitude of γ' for galaxies at low-velocity dispersion end than that in Poci et al. (2017), which may be due to the different sample selection criteria of the two surveys.

Since the hydrodynamical simulations may not reproduce perfectly the observed galaxy mass–size relation, the definition of half-light radius may not be referring to the same physical radius in observations and simulations. In Fig. 7, we further compare the total mass weighted density slope between simulated galaxies and our MaNGA sample within fixed radius of 3 and 5 kpc. Again, for fixed radius of 3 and 5 kpc, the simulations predict smaller γ' for galaxies with higher σ_v. The differences are more significant for Illustris and EAGLE simulations than that for TNG100 simulation.

4.2 Central versus satellite

In this project, we match the galaxies to the group catalogue derived by Yang et al. (2007, hereafter SDSSGC[5]). SDSSGC is constructed

[5]http://gax.shao.ac.cn/data/Group.html

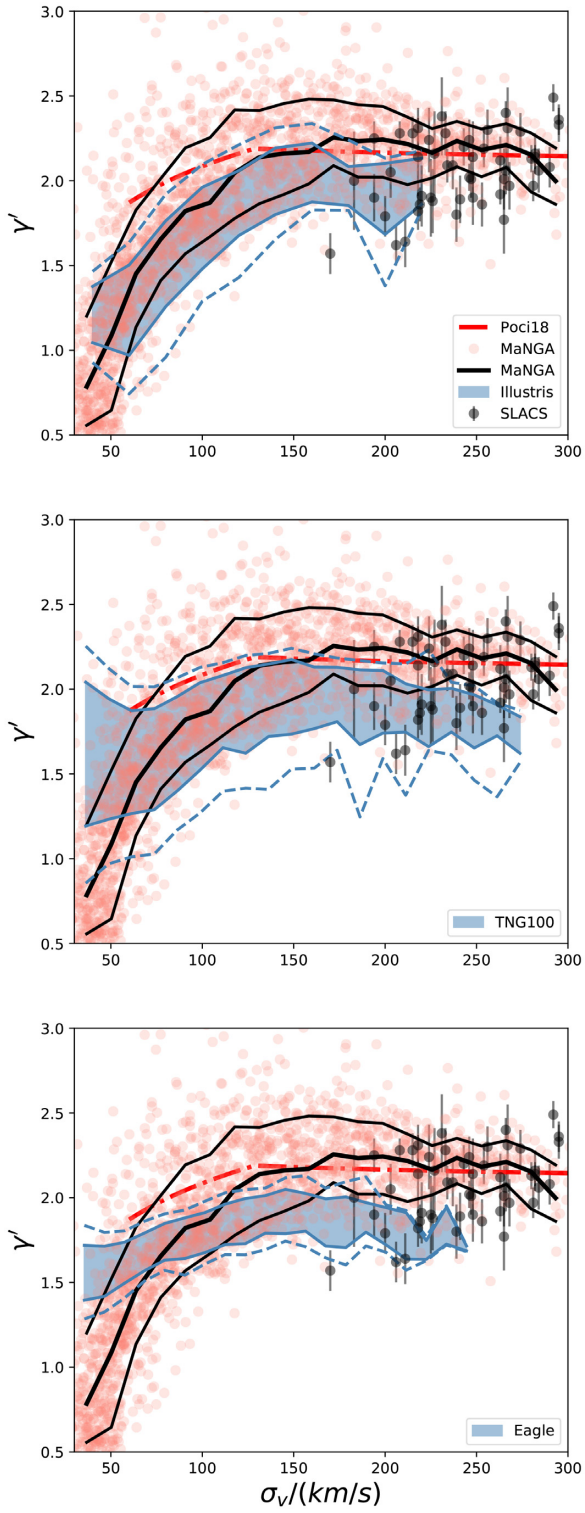

Figure 6. Red data points show observational results in this work. The mean and the region enclosing 70 per cent red points are shown with black solid lines. The black data points show γ' from strong lensing observation from (Auger et al. 2010). And the dashed line show the results from Poci et al. (2017). From top to bottom panels, we compare the results with Illustris, TNG100, and EAGLE simulations, respectively. The blue shading shows the region enclosing 70 per cent of the simulated galaxies and the dashed lines show the region enclosing 90 per cent simulated galaxies.

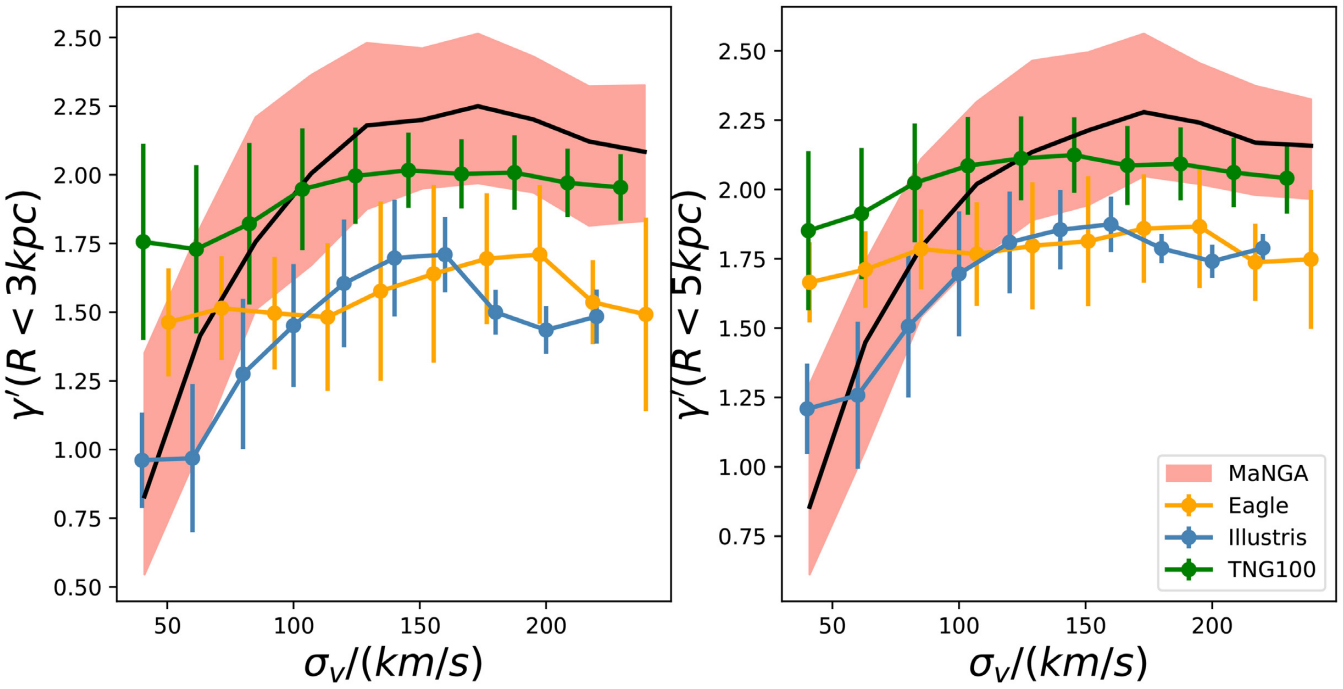

Figure 7. The figure shows the mass-weighted total density slopes within 3 kpc (left) and 5 kpc (right), respectively. The shadings show the regions enclosing 70 per cent observed galaxies and the black solid lines show the mean. The blue, green, and yellow lines show the mean γ–σ_v relation of Illustris, TNG100, and EAGLE simulations and the error bars show the region enclosing 70 per cent of simulated galaxies.

with the spectroscopic galaxy sample of SDSS-DR7 (Abazajian et al. 2009) using an adaptive halo-based group finder. Each galaxy in SDSS-DR7 is assigned to a group, and a halo mass is estimated for each group. We assume the central galaxy of each group is the one that has largest stellar mass.

For each galaxy in our MaNGA sample, we find its counterpart in the SDSSGC. Therefore, we can obtain its host halo mass, and we can tell whether it is a central galaxy or a satellite galaxy.

In Fig. 8, we select only the central galaxies from the MaNGA sample, and plot their total mass density slopes as a function of M_{200} of the groups. For groups with mass larger than $10^{13}\ h^{-1}\,\mathrm{M}_\odot$, their central galaxies are mostly early-type whose total mass density slope has a mean value 2.08 and a scatter of 0.27. For the lower mass groups, the central galaxy could be either early type or late type, and their total slopes scatter in a broad range from 1.5 to 2.75.

In Fig. 9, we show the total mass slope γ' for central galaxies and satellite galaxies using red and blue lines, respectively. The overall dependence of γ' on σ_v is similar for centrals and satellites. For galaxy with the similar σ_v, the amplitude of the mean γ' for satellites is higher than that of central by ∼0.1, which may be due to the fact that on average satellite galaxies form earlier in denser universe and have more concentrated stellar profiles.

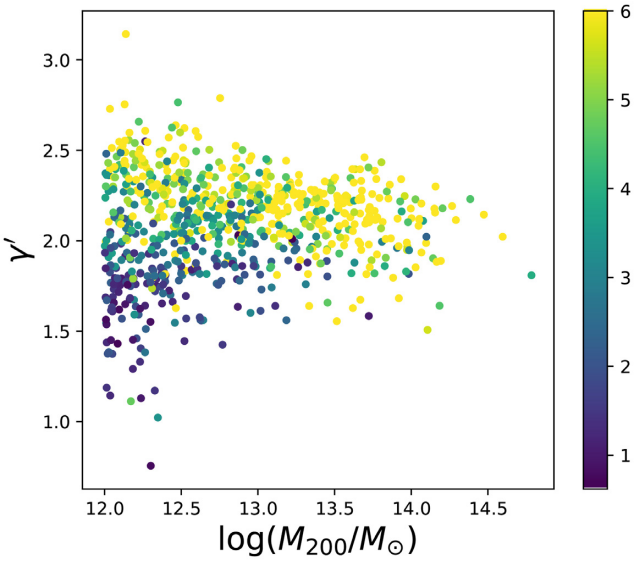

Figure 8. The figure shows the total mass density slope of the MaNGA galaxies as a function of M_{200} of their groups. We only plot the results for central galaxies. The colour of data points shows the Sérsic index of galaxies.

5 SUMMARY AND DISCUSSION

In this paper, we investigate the inner density profile of more than 2000 nearby galaxies from the SDSS-IV MaNGA survey. Our sample of galaxies is the largest of its kind, spanning 3 decades of stellar mass, and includes both early-type galaxies and late-type galaxies. Using IFU observations we derive γ', the mass-weighted total mass density slope within the effective radius, for these galaxies from the mass model built with the JAM method.

For galaxies with $\sigma_v > 100\ \mathrm{km\,s^{-1}}$, their mean density slopes hold almost a constant value of $\gamma' = 2.24$, decrease slowly with increasing of velocity dispersion, while for galaxies with $\sigma_v < 100\ \mathrm{km\,s^{-1}}$, the density slopes decrease rapidly with decreasing velocity dispersion.

We also investigate the relation between γ' and the stellar mass derived using stellar population synthesis models. We find the mean

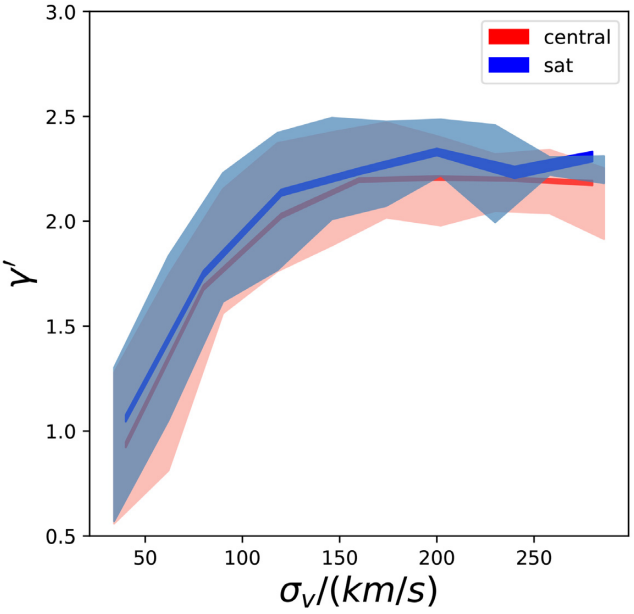

Figure 9. In Fig. 9, we show mean γ'–σ_v relation for central (red) and satellite (blue) galaxies, respectively. The line width shows the uncertainties of the mean γ'–σ_v relation. The shading show the regions enclosing 70 per cent of central (red) and satellite (blue) galaxies.

total density slopes is roughly constant for galaxies more massive than 10^{11} $M_\odot$ at a value of about 2.15. For these most massive galaxies, the dark matter only accounts for about 10 per cent of total mass budget within R_e, and their total density slopes are almost the same with their stellar mass density slopes. For galaxies less massive than 10^{11} $M_\odot$, the dark matter fraction increases with the decrease of the stellar mass, while the total density slopes decreases fast. Our results show that even if the scenario of bulge-halo conspiracy exists, it does not hold for a wide mass range.

For the same stellar mass, galaxies of larger sizes tend to have lower total density slopes. We find γ' increases with average stellar density within R_e, with slopes of 0.56 for galaxies with $\log(\Sigma_*^{SPS}/(M_\odot kpc^2)) < 8.9$ and 0.156 for galaxies $\log(\Sigma_*^{SPS}/(M_\odot kpc^2)) > 8.9$.

Interestingly, we find a large fraction of galaxies less massive than 10^{10} $M_\odot$ have total density slopes even shallower than 1. Given that the slopes of the luminosity of these galaxies are steep, our results imply density slopes shallower than 1 for the dark matter component within the R_e for these galaxies. The presence of a shallow dark matter density profile at the centre of dwarf galaxies has been reported by many previous studies for dwarf galaxies (Flores & Primack 1994; Moore 1994; McGaugh, Rubin & de Blok 2001; Marchesini et al. 2002; de Blok et al. 2008; Kuzio de Naray, McGaugh & de Blok 2008; Oman et al. 2015; Read, Walker & Steger 2019). On theoretical side, the cold dark matter numerical simulations always predict slopes close to 1 in absence of baryons. The apparent conflict has been known as 'core-cusp' problem. In reply to the observed cores, Navarro, Eke & Frenk (1996a) proposed the solution that the energy injections from supernovae feedback can cause the sudden remove of gas from centre of a cuspy dark matter halo, and the dark matter halo responds the change by transforming the cuspy centre to a core. The idea was further developed by others, showing that comparing with one single outburst of gas, a series of outburst driven by bursty star formation are more effective in generating the core (Gnedin & Zhao 2002; Read & Gilmore 2005; Mashchenko, Couchman & Wadsley 2006; Pontzen & Governato 2012; Teyssier et al. 2013). A host of simulations find cusp-core transformation occurs (Di Cintio et al. 2014; Oñorbe et al. 2015; Read, Agertz & Collins 2016; Tollet et al. 2016), while dark matter haloes remain cuspy in the others (Schaller et al. 2015; Genina et al. 2018; Bose et al. 2019). Researches based on hydrodynamical simulations show that the shallow dark matter density profile at the inner part of the halo may also closely relates to the star formation threshold density. A star formation threshold density higher than 1 cm^{-3} allows the gas to pile up at the centre of halo, so that an energetic feedback afterwards can efficiently blow out the gas and flatten the inner dark matter profile (also see Pontzen & Governato 2012; Benitez-Llambay et al. 2018; Dutton et al. 2018; Bose et al. 2019). The previous observations on core-cusp problem main focus on the dwarf galaxies with stellar mass below 10^9 solar masses, while our result imply the galaxies with higher mass may still possess shallow dark matter inner density profiles. A future detailed comparison of dwarf galaxy mass structures between observations and simulations will shed light on the subgrid feedback process in galaxy formation.

We compare our results with hydrodynamical simulations, EAGLE, Illustris, and TNG100. In all simulations, the total density γ' for galaxies with $\sigma_v > 150$ km s^{-1} are slightly below 2, shallower than our observed value of 2.24.

Finally, we explore the density slope dependence on their positions in groups/clusters, namely whether a galaxies is central galaxy or satellite galaxy. We divide our MaNGA galaxies into centrals and satellites using the SDSS group catalogue by Yang et al. (2007). For early-type central galaxies, the density slopes are about $\gamma' \sim 2.08$, and decreases slowly with increasing M_{200}. For late-type central galaxies, the density slope scatters in a wide range from 1.5 to 2.75. We also find that the amplitude of the γ'–σ_v relation for satellite galaxies is higher than that of centrals by 0.1.

ACKNOWLEDGEMENTS

We acknowledge National Natural Science Foundation of China (nos 11773032, 11390372, 1133303, 11821303, 11761131004) and National Key Program for Science and Technology Research and Development of China (2017YFB0203300). RL is supported by NAOC Nebula Talents Program and Newton mobility award. This work is partly supported by the National Key Basic Research and Development Program of China (no. 2018YFA0404501 to SM). SS is supported by grant ERC-StG-716532-PUNCA and STFC (grant nos ST/L00075X/1, ST/P000541/1).

We performed our computer runs on the Zen high performance computer cluster of the National Astronomical Observatories, Chinese Academy of Sciences (NAOC), and the Venus server at Tsinghua University. This research made use of Marvin, a core PYTHON package and web framework for MaNGA data, developed by Brian Cherinka, José Sánchez-Gallego, and Brett Andrews. (MaNGA Collaboration 2017).

Funding for the SDSS-IV has been provided by the Alfred P. Sloan Foundation, the U.S. Department of Energy Office of Science, and the Participating Institutions. SDSS-IV acknowledges support and resources from the Center for High-Performance Computing at the University of Utah. The SDSS web site is www.sdss.org.

SDSS-IV is managed by the Astrophysical Research Consortium for the Participating Institutions of the SDSS Collaboration including the Brazilian Participation Group, the Carnegie Institution for Science, Carnegie Mellon University, the Chilean Participa-

tion Group, the French Participation Group, Harvard-Smithsonian Center for Astrophysics, Instituto de Astrofísica de Canarias, The Johns Hopkins University, Kavli Institute for the Physics and Mathematics of the Universe (IPMU) / University of Tokyo, Lawrence Berkeley National Laboratory, Leibniz Institut für Astrophysik Potsdam (AIP), Max-Planck-Institut für Astronomie (MPIA Heidelberg), Max-Planck-Institut für Astrophysik (MPA Garching), Max-Planck-Institut für Extraterrestrische Physik (MPE), National Astronomical Observatories of China, New Mexico State University, New York University, University of Notre Dame, Observatário Nacional / MCTI, The Ohio State University, Pennsylvania State University, Shanghai Astronomical Observatory, United Kingdom Participation Group, Universidad Nacional Autónoma de México, University of Arizona, University of Colorado Boulder, University of Oxford, University of Portsmouth, University of Utah, University of Virginia, University of Washington, University of Wisconsin, Vanderbilt University, and Yale University.

REFERENCES

Abazajian K. N. et al., 2009, ApJS, 182, 543
Abolfathi B.et al., 2018, ApJS, 235, 42
Auger M. W., Treu T., Bolton A. S., Gavazzi R., Koopmans L. V. E., Marshall P. J., Moustakas L. A., Burles S., 2010, ApJ, 724, 511
Benítez-Llambay A., Navarro J. F., Frenk C. S., Ludlow A. D., 2018, MNRAS, 473, 1019
Binney J., Tremaine S., 1987, Galactic Dynamics, Princeton Univ. Press, Princeton, NJ
Blanton M. R. et al., 2017, AJ, 154, 28
Blumenthal G. R., Faber S. M., Flores R., Primack J. R., 1986, ApJ, 301, 27
Bose S. et al., 2019, MNRAS, 486, 4790
Bruderer C., Read J. I., Coles J. P., Leier D., Falco E. E., Ferreras I., Saha P., 2016, MNRAS, 456, 870
Bryant J. J. et al., 2015, MNRAS, 447, 2857
Bundy K. et al., 2015, ApJ, 798, 7
Cappellari M., 2002, MNRAS, 333, 400
Cappellari M., 2008, MNRAS, 390, 71
Cappellari M., 2016, ARA&A, 54, 597
Cappellari M., 2017, MNRAS, 466, 798
Cappellari M., Copin Y., 2003, MNRAS, 342, 345
Cappellari M., Emsellem E., 2004, PASP, 116, 138
Cappellari M. et al., 2011, MNRAS, 416, 1680
Cappellari M. et al., 2013, MNRAS, 432, 1709
Courteau S., Dutton A. A., 2015, ApJ, 801, L20
Crain R. A. et al., 2015, MNRAS, 450, 1937
de Blok W. J. G., Walter F., Brinks E., Trachternach C., Oh S.-H., Kennicutt R. C., 2008, AJ, 136, 2648
Dehnen W., 2005, MNRAS, 360, 892
Di Cintio A., Brook C. B., Dutton A. A., Macciò A. V., Stinson G. S., Knebe A., 2014, MNRAS, 441, 2986
Drory N. et al., 2015, AJ, 149, 77
Duffy A. R., Schaye J., Kay S. T., Dalla Vecchia C., Battye R. A., Booth C. M., 2010, MNRAS, 405, 2161
Dutton A. A., Treu T., 2014, MNRAS, 438, 3594
Dutton A. A., Macciò A. V., Buck T., Dixon K. L., Blank M., Obreja A., 2019, MNRAS, 486, 655
Emsellem E., Monnet G., Bacon R., 1994, A&A, 285, 723
Flores R. A., Primack J. R., 1994, ApJ, 427, L1
Foreman-Mackey D., Hogg D. W., Lang D., Goodman J., 2013, PASP, 125, 306
Genel S. et al., 2014, MNRAS, 445, 175
Genina A. et al., 2018, MNRAS, 474, 1398
Gnedin O. Y., Zhao H., 2002, MNRAS, 333, 299
Gnedin O. Y., Kravtsov A. V., Klypin A. A., Nagai D., 2004, ApJ, 616, 16
Gunn J. E. et al., 2006, AJ, 131, 2332
Gustafsson M., Fairbairn M., Sommer-Larsen J., 2006, Phys. Rev. D, 74, 123522
He Q. et al., 2019, preprint (arXiv:1907.01680)
Huang S. et al., 2018, preprint (arXiv:1811.01139)
Jeans J. H., 1922, MNRAS, 82, 122
Koopmans L. V. E. et al., 2009, ApJ, 703, L51
Kuzio de Naray R., McGaugh S. S., de Blok W. J. G., 2008, ApJ, 676, 920
La Barbera F., de Carvalho R. R., de La Rosa I. G., Lopes P. A. A., Kohl-Moreira J. L., Capelato H. V., 2010, MNRAS, 408, 1313
Law D. R. et al., 2015, AJ, 150, 19
Law D. R. et al., 2016, AJ, 152, 83
Lelli F., McGaugh S. S., Schombert J. M., 2016, AJ, 152, 157
Li H., Li R., Mao S., Xu D., Long R. J., Emsellem E., 2016, MNRAS, 455, 3680
Li H. et al., 2018, MNRAS, 476, 1765
Ma C.-P., Greene J. E., McConnell N., Janish R., Blakeslee J. P., Thomas J., Murphy J. D., 2014, ApJ, 795, 158
Marchesini D., D'Onghia E., Chincarini G., Firmani C., Conconi P., Molinari E., Zacchei A., 2002, ApJ, 575, 801
Marinacci F. et al., 2018, MNRAS, 480, 5113
Mashchenko S., Couchman H. M. P., Wadsley J., 2006, Nature, 442, 539
McGaugh S. S., Rubin V. C., de Blok W. J. G., 2001, AJ, 122, 2381
Moore B., 1994, preprint (astro-ph/9402009)
Naiman J. P. et al., 2018, MNRAS, 477, 1206
Navarro J. F., Eke V. R., Frenk C. S., 1996a, MNRAS, 283, L72
Navarro J. F., Frenk C. S., White S. D. M., 1996b, ApJ, 462, 563
Navarro J. F., Frenk C. S., White S. D. M., 1997, ApJ, 490, 493
Nelson D. et al., 2015, A&C, 13, 12
Nelson D. et al., 2018, MNRAS, 475, 624
Nelson D. et al., 2019,ComAC, 6, 2
Newman A. B., Ellis R. S., Treu T., 2015, ApJ, 814, 26
Oman K. A. et al., 2015, MNRAS, 452, 3650
Oñorbe J., Boylan-Kolchin M., Bullock J. S., Hopkins P. F., Kereš D., Faucher-Giguère C.-A., Quataert E., Murray N., 2015, MNRAS, 454, 2092
Pillepich A. et al., 2018, MNRAS, 475, 648
Poci A., Cappellari M., McDermid R. M., 2017, MNRAS, 467, 1397
Pontzen A., Governato F., 2012, MNRAS, 421, 3464
Read J. I., Gilmore G., 2005, MNRAS, 356, 107
Read J. I., Agertz O., Collins M. L. M., 2016, MNRAS, 459, 2573
Read J. I., Walker M. G., Steger P., 2019, MNRAS, 484, 1401
Salpeter E. E., 1955, ApJ, 121, 161
Sánchez-Blázquez P. et al., 2006, MNRAS, 371, 703
Sánchez S. F., Kennicutt R. C., Gil de Paz A., van de Ven G., Vílchez J. M., Wisotzki L., 2012, A&A, 538, A8
Schaller M. et al., 2015, MNRAS, 451, 1247
Schaye J. et al., 2015, MNRAS, 446, 521
Smee S. A., Gunn J. E., Uomoto A., Roe N., Schlegel D., Rockosi C. M., Carr M. A., Leger F., 2013, AJ, 146, 32
Sonnenfeld A., Treu T., Gavazzi R., Suyu S. H., Marshall P. J., Auger M. W., Nipoti C., 2013, ApJ, 777, 98
Sonnenfeld A., Leauthaud A., Auger M. W., Gavazzi R., Treu T., More S., Komiyama Y., 2018, MNRAS, 481, 164
Springel V. et al., 2018, MNRAS, 475, 676
Teyssier R., Pontzen A., Dubois Y., Read J. I., 2013, MNRAS, 429, 3068
Tollet E. et al., 2016, MNRAS, 456, 3542
Tortora C., La Barbera F., Napolitano N. R., Romanowsky A. J., Ferreras I., de Carvalho R. R., 2014, MNRAS, 445, 115
Tortora C., La Barbera F., Napolitano N. R., 2016, MNRAS, 455, 308
Tortora C., Posti L., Koopmans L. V. E., Napolitano N. R., 2019, MNRAS, 498, 5483

Vazdekis A., Sánchez-Blázquez P., Falcón-Barroso J., Cenarro A. J., Beasley M. A., Cardiel N., Gorgas J., Peletier R. F., 2010, MNRAS, 404, 1639
Vogelsberger M. et al., 2014a, MNRAS, 444, 1518
Vogelsberger M. et al., 2014b, Nature, 509, 177
Wake D. A. et al., 2017, AJ, 154, 86
Wasserman A. et al., 2018, ApJ, 863, 130
Westfall K. B. et al., 2019, preprint (arXiv:1901.00856)
Yan R., Tremonti C., Bershady M. A., Law D. R., Schlegel D. J., Bundy K., Drory N., MacDonald N., 2016a, AJ, 151, 8
Yan R., Bundy K., Law D. R., Bershady M. A., Andrews B., Cherinka B., Diamond-Stanic A. M., 2016b, AJ, 152, 197
Yang X., Mo H. J., van den Bosch F. C., Pasquali A., Li C., Barden M., 2007, ApJ, 671, 153

APPENDIX A: MASS MODEL DEPENDENCE

In our fiducial model, we assume the stellar mass distribution follows the light distribution and the dark matter halo follows an NFW profile. To explore whether our results depend on the choice of mass model, we perform JAM with an axisymmetric double power-law model:

$$\rho_{\rm tot}(l) = \rho_{\rm s} \left(\frac{l}{l_{\rm s}}\right)^{\gamma} \left(\frac{1}{2} - \frac{1}{2}\frac{l}{l_{\rm s}}\right)^{-\gamma-3}, \quad \text{(A1)}$$

where the ellipsoid radius $l = \sqrt{R^2 + z^2/q^2}$, where z-axis is the symmetric axis, and R is the transverse radius; Free parameters q, $l_{\rm s}$, and $\rho_{\rm s}$ are the intrinsic axial ratio, scale radius, and density at the scale radius, respectively. In this model, we do not split density into light and dark when calculating the gravitational potential. For light density tracer, we still use the same MGEs as our fiducial model.

In Fig. A1, we compare the mass-weighted total density slope and the total mass within $R_{\rm e}$. One can find that the recovered values of total mass within the effective radius from two models agree well with each other. Two different mass models also produce consistent total density slope. Although the dispersion increases slightly for galaxies with $\gamma' > 2$, but the results for the majority of the galaxies still agree between the two models. Thus, we assert that our conclusions in this paper are not affected by the detailed choice of parametrization.

APPENDIX B: MOCK TEST

In Li et al. (2016), we have assessed the effectiveness of the JAM technique with the cosmological hydrodynamical simulation from Illustris project (Genel et al. 2014; Vogelsberger et al. 2014a,b; Nelson et al. 2015). We have made use of the Illustris-1 (L75n1820FP) simulation box in the Illustris project that contains 1802^3 particles for dark matter and about the same number of cells for gas or star particles. The size of box is 106.5 Mpc on a side, and the softening lengths for dark matter and baryon components are 1420 and 710 pc, respectively.

For a selected galaxy in the simulation, we projected its stellar particles on a two-dimensional grid cells of $2 \times 2\ h^{-2}$ kpc^2, comparable to the physical size covered by a single MaNGA fibre. The mean line-of-sight velocity and velocity dispersion of each cell was obtained by calculating the stellar-mass-weighted mean and standard deviation of the line-of-sight velocity of the star particles in each cell. We set the 'observational' uncertainties of $v_{\rm rms}$ to be proportional to the intrinsic Poisson error of the velocity of each cell, but scaled to the uncertainty level of 40 km s^{-1}, which is similar to a typical galaxy in CALIFA survey (Sánchez et al. 2012). The surface brightness of each cell was obtained by dividing total luminosity of the star particles in the cell by the area of the cell where we assumed a constant mass-to-light ratio of 1. Only the data within a radius of $2.5R_{\rm e}$ were used in the fitting.

In Li et al. (2016), we selected 1400 galaxies from Illustris simulation, with a stellar mass $M_* > 10^{10}$ M$_\odot$. We find the total mass within $2.5R_{\rm e}$ can be recovered with a accuracy of $\Delta M_{\rm tot}/M_{\rm tot} = 0.02^{+0.14}_{-0.17}$. Fig. B1 shows the recovery of the total

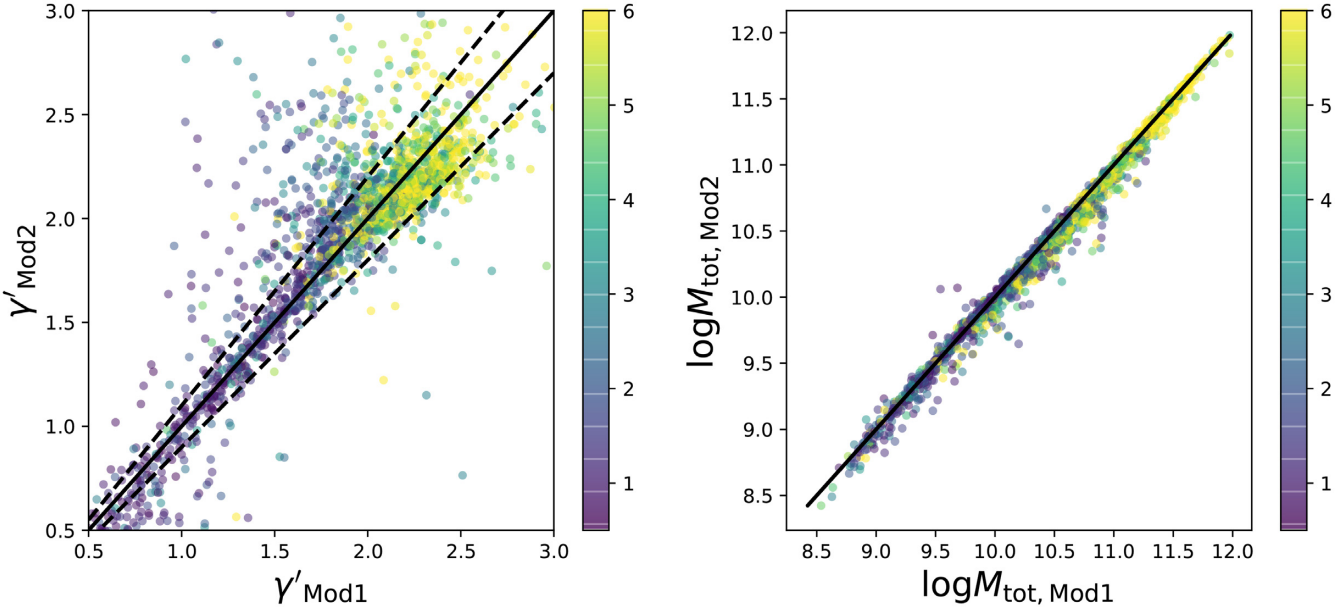

Figure A1. In the left-hand panel, we compare the recovered γ' from our fiducial model (Mod1) and axisymmetric double power-law model (Mod2). The solid line shows $y = x$, and the 10 per cent scattering region is shown by two dashed lines. The colour represents the Sérsic index of the galaxies. In the right-hand panel, we compare the total mass within the effective radius from the two models.

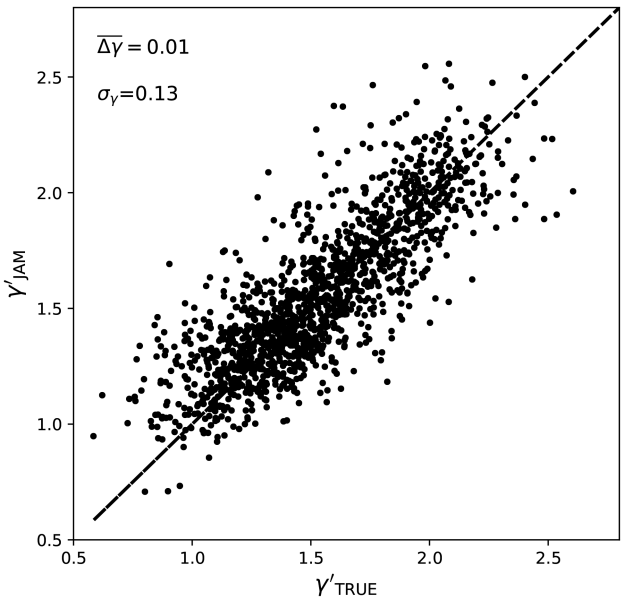

Figure B1. The figure shows the JAM recovery of γ' for galaxies in the illustris simulation. We derive the slopes using the same mass models as that in Li et al. (2016).

density slopes of the selected galaxies. We found the mean error of the recovered γ' is only 1 per cent, with a scatter of 13 per cent.

One caveat of our previous analysis is that we assume the observations data extend to $2.5R_{\rm e}$, while most of the galaxies from MaNGA are only covered by the IFU bundle within $1.5R_{\rm e}$ or $R_{\rm e}$. Below, we show the results of JAM analysis on a couple of random-selected galaxies in Illustris-I simulation, following the same method described in Li et al. (2016), but with data only covering the region within $R_{\rm e}$. We find the total density slopes can still be well constrained, with an uncertainty level of $\sim$ 15 per cent for γ'. In Fig. B2, we show four examples of the mock test, including galaxies of different masses and different intrinsic stellar density slopes. One can find that the total density slopes of these galaxies are well recovered within $R_{\rm e}$.

APPENDIX C: DEPENDENCE ON THE NUMBER OF VORONOI BINS

Before deriving the kinematic information from spectrum fitting, the MaNGA data cubes are Voronoi binned (Cappellari & Copin 2003) to an S/N = 10, which may introduce a spatial smoothing effect to the kinematic data. To test the dependence of results on the number of Voronoi bins, we have tried a criteria of S/N = 60 for binning and find the results does not change. To further explore the effect of binning, we run our JAM analysis on a simulated galaxy from Illustris simulation (mock observation extend to $R_{\rm e}$).

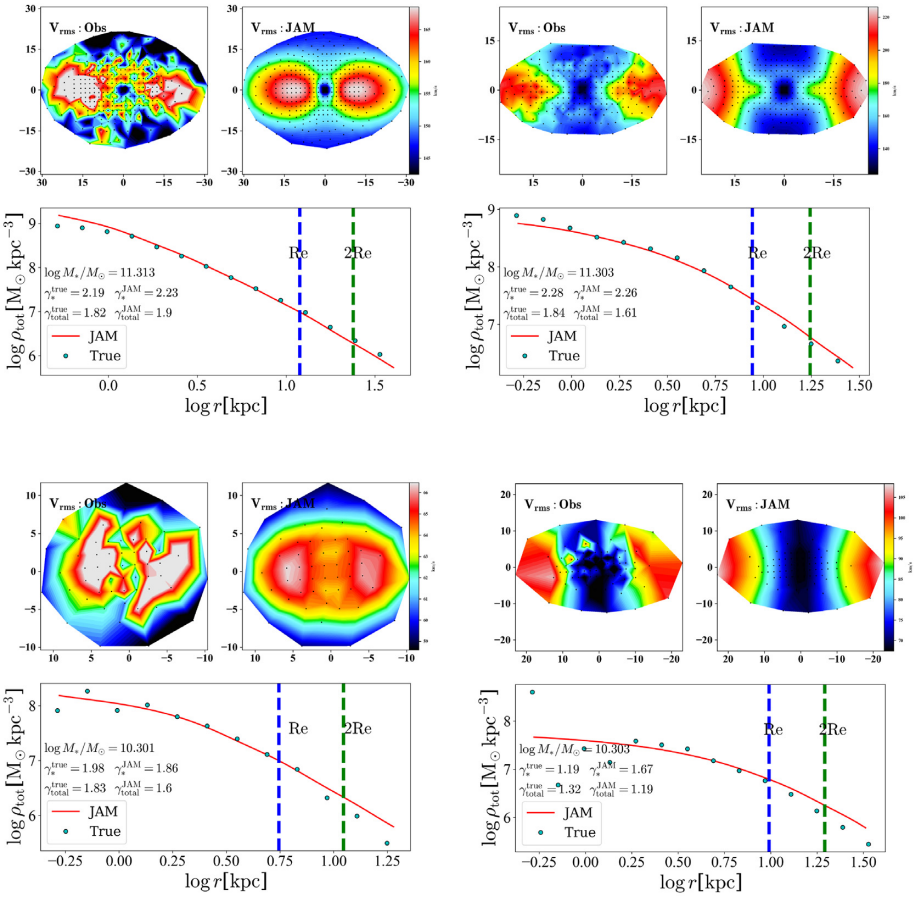

Figure B2. The figure shows recovery results for four galaxies in the Illustris simulation. In each subplot, the upper panel shows the comparison between the $v_{\rm rms}$ distribution of the mock observation and that of the JAM recovered model. In the lower panel, we compare the density profile measured from particle data of the simulated galaxy (green dot) and that of the JAM recovered model (red solid line), and we also show in text the input and recovered γ' and γ_*.

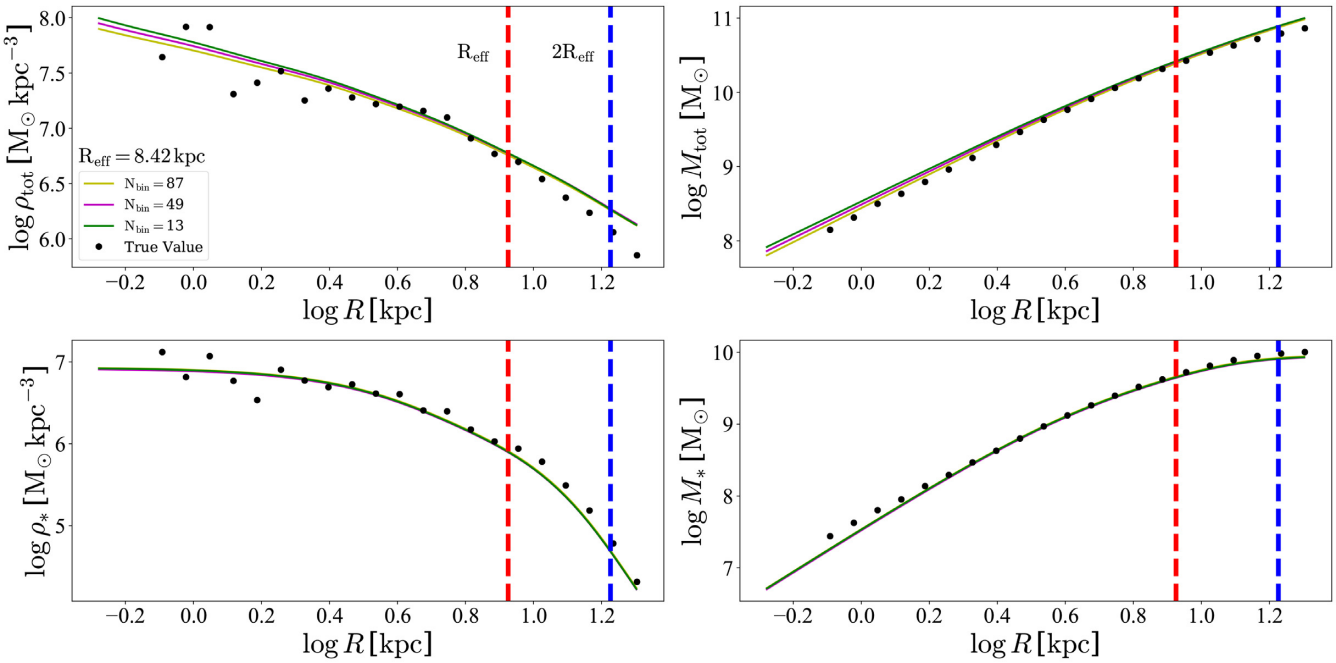

Figure C1. The figure shows the recovery of the total density profile (top left), the stellar density profile (bottom left), the total mass enclosed within R (top right), and the total stellar mass within R (bottom right) for a simulated galaxy from Illustris simulation. The vertical lines show the position of $R_{\rm e}$ and $2R_{\rm e}$. In each figure, different lines show the results using different number of Voronoi bins.

We Voronoi bin the velocity grids with three different S/N criteria. The numbers of bins within $R_{\rm e}$ are 13, 49, and 87. For each binned data set, we perform the JAM analysis. In Fig. C1, we show the recovery of the total density profile (top left), the stellar density profile (bottom left), the total mass enclosed within R (top right), and the total stellar mass within R (bottom right) for different binning conditions. We find the recovery of the mass model of a galaxy are not affected by the choice of number of Voronoi bins.

This paper has been typeset from a TEX/LATEX file prepared by the author.